SSRG International Journal of Mechanical Engineering
ISSN: 2348-8360/ https://doi.org/10.14445/23488360/IJME-V13I3P105

Volume 13 Issue 3, 54-67, March 2026

Original Article

HAM-Guided Physics-Informed Neural Operator for Stratified Oldroyd-B and Maxwell Nanofluid Flow with Radiation and Gyrotactic Microorganisms

D. Vidhya[1], P. Uma Devi[2]

[1]*Department of Mathematics, Dr. N.G.P. Institute of Technology, Coimbatore, Tamil Nadu, India.*
[2]*Department of Mathematics, Dr. N.G.P. Arts and Science College, Coimbatore, Tamil Nadu, India.*

[1]*Corresponding Author : vidhyad222@gmail.com*

Received: 22 December 2025 Revised: 25 January 2026 Accepted: 21 February 2026 Published: 28 March 2026

Abstract *- Stratified Oldroyd-B and Maxwell nanofluid flows over a stretching sheet with radiation and gyrotactic microorganisms are addressed in this work by creating a HAM-guided physics-informed neural operator, in accordance with the components and aims outlined in the cited study. A Homotopy Analysis Method (HAM) is used to transform the coupled PDE system into a nonlinear ODE boundary-value problem in the baseline formulation, which employs similarity reduction. Data-driven prediction and regression-based error analysis are provided by an Artificial Neural Network (ANN) trained with Levenberg-Marquardt. In order to enhance generalisability, to keep this physics but train an operator that maps (η, "parameters")→(f^',θ,ϕ,χ) in both fluids, with the Maxwell case included by the documented switch De_2=0. The results display that, in a radiation+stratification scenario (C3), the suggested approach produces wall metrics f^'' (0)=1.245, -^' (0)=0.612, -ϕ^' (0)=0.428, and -χ^' (0)=0.317, which are comparable to physics solvers and an improvement over an ANN baseline that is solely based on data. The prediction accuracy is high across all fields (R^2≥0.9983) and RMSE ≈0.003-0.005 across all C1–C8 observations. Sweeps are efficient because, following training (which takes about 18 minutes), inference takes about 3.2 milliseconds per case, which allows for quick sensitivity studies while maintaining the stratification trend that decreases mass and heat transfer.*

Keywords *- Homotopy Analysis Method, Artificial Neural Network, Levenberg–Marquardt, Maxwell nanofluid flow, Gyrotactic microorganisms.*

1. Introduction

For high-gradient transport near stretched surfaces in coating, extrusion, polymer processing, and bio-thermal microflows, a realistic modelling base is provided by non-Newtonian nanofluids with stratification, radiation, and microorganism-induced bioconvection [1]. The divergence in relaxation/retardation structure between Oldroyd-B and Maxwell fluids, which alters the near-wall momentum diffusion and coupled thermal/solutal responses to the same boundary forcing, makes their comparative behavior all the more important. Both fluids capture viscoelastic memory. The presented research presents a two-dimensional, incompressible stratified boundary-layer flow over a stretching sheet as a physical problem. It incorporates radiation, thermophoresis, Brownian motion, Cattaneo-Christov dual heat and mass fluxes, and gyrotactic microorganisms. The Maxwell case is maintained under the same physical conditions to emphasise model-dependent variability in flow, heat transfer, and nanoparticle dynamics.

In order to evaluate the coupled momentum-energy-species-microorganism system on a semi-infinite similarity domain [7], the document's methodology relies on a technique that converts the governing PDE system into a similarity-reduced ODE boundary-value problem. Temperature, nanoparticle concentration, and microorganism density all change linearly along the streamwise direction in the flow formulation, which embeds stratification directly into boundary conditions [9]. The configuration of the stretching wall, velocity components, and stratified wall/ambient states are all explicitly defined [8]. Radiative heat contribution, dual relaxation (temporal delay) encoded through the Cattaneo-Christov model [10], and cross-diffusion factors due to thermophoresis and Brownian motion are the competing mechanisms that drive transport in the reduced system.

The HAM is used analytically to solve transformed Ordinary Differential Equations (ODEs) in this study. HAM is well-suited to nonlinear boundary-layer problems on semi-infinite domains due to its controlled convergence via initial guesses and linear operators, which makes it an ideal choice for solution generation. The document goes beyond just creating profiles. It uses an ANN strategy (with Levenberg-Marquardt optimisation) to forecast the responses of velocity,

temperature, and concentration under various parameter scenarios. It places an emphasis on regression/error plots and MSE diagnostics using training/validation/testing partitions. The necessity to quickly assess profiles across several physical variables without performing an expensive analytical or numerical method repeatedly drove the development of this "solve + learn" approach. The document also makes note of the fact that turning off the retardation parameter (written as De_2) transforms Oldroyd-B into Maxwell, allowing for side-by-side assessment with matched inputs, demonstrating that the comparison between Oldroyd-B and Maxwell is operationally clean.

From a transport perspective, the study found that thermal and solutal stratification reduce mass and heat transfer, relaxation-related characteristics hinder fluid motion, and mixed convection can improve it. These effects should be maintained by any physical reliability surrogate model. Expanding on this idea, the suggested structure in Section 3 improves upon the current HAM+ANN concept by learning all possible solutions as a parameter-aware operator (instead of just fitting discrete cases), all the while maintaining the same physics of similarity ODEs and the same comparative Oldroyd-B Maxwell switch. In addition to supporting robust wall-metric computation and improving scalability for parameter sweeps, this also fits in well with the document's focus on error management and diagnostics of regression quality.

Despite the availability of analytical, semi-analytical, and numerical methods for Maxwell and Oldroyd-B nanofluid flows, most research solves the boundary-layer equations for a predetermined set of physical parameters. Classical methods such as the Homotopy Analysis Method, shooting-based Runge–Kutta schemes, and bvp4c solvers provide precise solutions but require repetitive calculations as the parameter space changes, making large-scale parametric analysis computationally expensive. Recent artificial neural network–based regression models enhance prediction speed but are trained for discrete examples and do not learn the controlling nonlinear system's solution operator. Thus, they cannot handle stratification, radiation, viscoelastic relaxation, Brownian diffusion, thermophoresis, and microbe transport simultaneously. Most studies analyse Oldroyd-B and Maxwell fluids separately rather than as a parametric family, making it difficult to compare them under equivalent physical conditions.

Existing nanofluid bioconvection with Cattaneo–Christov dual flux works mostly use numerical or series-based solutions and do not provide a reusable physics-consistent surrogate that can predict wall transport quantities instantly for design-oriented applications. Engineering requires rapid evaluation of skin friction, heat transfer, mass transfer, and microbe flow across a large parameter domain for coating process optimisation and control, polymer extrusion, bio-thermal systems, and microfluidic transport.

HAM-guided physics-informed neural operators that learn the whole family of similarity solutions as a function of the controlling physical parameters are developed in this study to overcome these constraints. The suggested approach minimises repeating boundary-value issue solutions while maintaining physical consistency by embedding similarity-reduced transport physics within the learning framework and leveraging HAM as a convergence-controlled instructor. This allows fast and precise comparison of stratified Oldroyd-B and Maxwell nanofluids under identical conditions and scaled parametric research.

Breakdown of remaining paper sections: Section 2 includes related literature; Methodology is explained in Section 3. Results analysis is in Section 4, and conclusions are in Section 5.

2. Related Works

The primary emphasis of Chouhan, N. et al. [11] is on the Maxwell nanofluid flow over an exponentially stretchable surface accompanied by magnetic energy and thermal input. A two-dimensional model involving gyrotactic microbes is also taken into account, along with motion, in the presence of heat radiation and fluid loss. By including the relevant translation variables, the nonlinear governing models are transformed into ordinary differential models. Utilising the bvp4c technique in MATLAB, the remodelled equations are numerically computed. Speed, temperature, nanofluid concentration, microbe profiles, skin friction coefficient, Nusselt, and density numbers are all examined in relation to physical properties. In addition, results showed that by increasing the values of the material and magnetic characteristics, the fluid velocity actually decreases. New concentration and temperature profiles of nanofluids are generated by the thermophoresis parameter. There is a decrease in the microbial profile as the Peclet and Lewis populations are increased. Energy and mass are transferred more efficiently with the radiation parameter. When the Peclet number is present, the motile density number increases as the quantity of the microorganism difference parameter increases.

The model presented by Alsallami, S. A., et al. [12] is based on a set of Partial Differential Equations (PDEs) formed by the Maxwell and Navier-Stokes equations. Through the application of a similarity framework, the system of modelled equations has been simplified to the usual system of dimensionless differential equations. The numerical technique boundary value solver (bvp4c) was used to generate the answers for the problem's quantitative approximation. Displayed and addressed are the physical quantities that result from the modelled equations. The heat transmission rate is thought to be enhanced by the Prandtl number and the radiation effect, and the velocity field is thought to be

diminished by the improvement of the magnetic parameter. Chemical reactions, temperature differentials, concentration ratios, and the Schmidt number all have an impact that grows as the entropy rate, and the Bejan number do as well.

Heat transfer rate, mass, and velocity of Maxwell nanofluid movement in a sensor surface vertical channel formed by two infinite parallel plates are the variables that Salahuddin, T. et al. [13] rely on. The Buongiorno nanofluid model is utilised to derive the mass and heat transport equations, as researchers across the globe strive to improve the utilisation of nanofluids in various industrial contexts. Since mixed convection flows produce various transport mechanisms in engineering systems, studying natural convection and its effects on Maxwell fluid flow is a common practice. In addition, many industrial fields find the examination of Brownian Dufin variables for such a scenario. By employing suitable modified transformations, a nonlinear system of differential equations can be derived. The problem is solved using a numerical approach. The dimensionless parameters are illustrated and explained for the relevant profiles. The results demonstrate that the fluid's velocity field decreases due to buoyancy forces acting against its motion. The momentum boundary layer fades as the permeability velocity, Maxwell number, and variable viscosity parameter increase. When it comes to thermophoresis parameters and Brownian diffusion, the inverse is true. As the Brownian diffusion parameter increases, the thermal boundary layer experiences an enhancement, while the concentration field exhibits a decrease. The Dufin effect and Soret factor make the temperature-concentration graph steeper.

The authors Habib, D., et al. [14] first converted the flow equations to their equivalent one-dimensional Ordinary Differential Equations (ODEs), and then they utilised the shooting technique to convert these ODEs into a linear form. Using the Runge-Kutta order 4 approach, the computational software MATLAB makes use of both the numerical and graphical results. To show numerical and graphical results of profiles of motile density, concentration, micro-rotation, temperature, and velocity. With increasing levels of magnetic parameter, the micro-rotational profile twists while the velocity profile decreases. A decrease in the motile density profile is observed when the numbers of Lewis and Peclet are increased. As the values of the thermophoresis parameters, the Rayleigh number, and the Brownian motion were increased, the temperature distribution was also expanded.

Examining Maxwell nanofluid through an expanding permeable surface in relation to the activation energy is the goal of Thumma, T. et al. [15]. The exceptional viscoelastic behavior is a defining feature of the Maxwell nanofluid. The transport phenomena also provide light on the combined function of surface conditions for heat flow and slip velocity. Critical to chemical reactions and energy conversion are the cross-diffusion processes involving Brownian motion and energy. By applying super-imposing similarity principles, the sophisticated model that comes with dimensional quantities becomes dimensionless. In addition, the Adomian decomposition method, a strong semi-analytical tool, is used to implement the combined impacts of these components. With validation of particular circumstances, the physical features of the proposed factors are obtained and graphically depicted together with their numerical findings. But the study's main takeaways are that Brownian and thermophoresis both work to improve the fluid's temperature distribution, and that increased elasticity for the Deborah number's appearance reduces the fluid's velocity, which is a regulating parameter.

The magnetohydrodynamic flow of a Maxwell nanofluid stretching surface in a porous medium was studied by Afridi, M. I., et al. [16] using a new technique based on Artificial Neural Networks, taking into consideration heating, among other physical phenomena. Thermophoresis and Brownian motion were examined for their impact on the nanofluid's temperature and concentration fields. The boundary layer equations up to the second level of truncation have been formulated using the local non-similarity methodology in order to compute the solutions of non-similar boundary layer equations. A novel neural network called a Levenberg-Marquardt Backpropagation is used to solve the system. By providing precise answers for distributions of nanoparticle concentration, temperature, and velocity across a wide range of physical parameters, the model based on Artificial Neural Networks outperformed traditional numerical methods, improving both accuracy and efficiency. The study proved that thermal radiation, electromagnetic fields, and Darcy-Forchheimer effects had a major impact on the dynamics of flows and the rates of heat transfer. This method, which is based on Artificial Neural Networks, has great potential for solving complex fluid dynamics problems; it speeds up computations and improves accuracy compared to older methods, allowing for more sophisticated modelling of nanofluid flows in different heat management schemes. Several parameters are directly related to the temperature profile: porosity, thermal radiation, heat generation/absorption, and temperature ratio. The concentration profile becomes steeper as the thermophoresis parameter's value rises, and it becomes flatter as the Brownian motion proceeds.

Recent developments [17] in operator-learning have significantly advanced the solution of parametric partial differential equations. Physics-informed neural operators have been successfully applied to coupled forward–backward PDE systems, turbulent-flow control, and nonlinear multi-physics problems, demonstrating strong generalisation across varying initial conditions and parameter spaces. These models combine the discretisation-invariant learning capability of neural operators with physics-based residual constraints, enabling fast and mesh-independent prediction of solution fields. In particular, recent PINO solvers have shown the

ability to operate with limited or even no labelled data by enforcing governing equations during training, while hybrid training strategies have been introduced to improve convergence and extrapolation in stiff systems. Furthermore, physics-informed operator frameworks have been extended to complex geometries and real-time control applications, highlighting their potential for large-scale scientific computing and digital-twin modelling.

Analytical, semi-analytical, and numerical methods for Maxwell and Oldroyd-B nanofluid flows are available; most research solves boundary-layer equations for preset physical parameters. Classical approaches like the Homotopy Analysis Method, shooting-based Runge–Kutta schemes, and bvp4c solvers provide exact solutions but require repetitive calculation as the parameter space evolves, making large-scale parametric analysis computationally expensive. Recent artificial neural network–based regression models improve prediction speed but only learn discrete examples and not the controlling nonlinear system's solution operator. Therefore, they cannot manage stratification, radiation, viscoelastic relaxation, Brownian diffusion, thermophoresis, and microbe movement concurrently. The parametric family of Oldroyd-B and Maxwell fluids is rarely studied, making it impossible to compare them under identical physical conditions.

Existing nanofluid bioconvection with Cattaneo–Christov dual flux works generally use numerical or series-based solutions and do not give a reusable physics-consistent surrogate that can forecast wall transport quantities instantaneously for design-oriented applications Engineering demands rapid evaluation of skin friction, heat transfer, mass transfer, and microbe flow across a vast parameter domain for coating process optimisation and control, polymer extrusion, bio-thermal systems, and microfluidic transport.

Physics-Informed Neural Operators (PINO) have succeeded in fluid dynamics issues with recent improvements. Recently, [18, 19] have used PINOs to turbulent flow fields and reactive transport issues, demonstrating that operator learning can generalise across parameter regimes. Most of these investigations use Newtonian fluids or classical PDE systems without viscoelastic effects. Although fundamental, these methods do not handle stratified Oldroyd-B or Maxwell nanofluid flows. PINO models generally lack HAM-guided initialisation. In work employs HAM as a guide and focuses on coupled nonlinear ODE systems from stratified, non-Newtonian nanofluids with radiation and bioconvection, expanding the PINO approach.

This study develops HAM-guided physics-informed neural operators that learn all similarity solutions as a function of the governing physical parameters to overcome these limits. Embedding similarity-reduced transport physics in the learning framework and using HAM as a convergence-controlled instructor reduces boundary-value issue solutions while retaining physical consistency. This enables fast, exact comparison of stratified Oldroyd-B and Maxwell nanofluids under identical conditions and a scaled parametric study.

Homotopy Analysis Method and Physics-Informed Neural Operator (HG-PINO) are used in this study to improve on previous work. Recent PINO studies have focused on simpler PDE systems, while the HG-PINO framework tackles complex stratified Oldroyd-B and Maxwell nanofluid flows. The unique approach is to use HAM as a solution technique and operator "teacher" to ensure convergence and physics-consistent learning. For a unified comparison of viscoelastic effects, to explicitly handle Oldroyd-B and Maxwell fluids under the same parametric domain. This contrasts with previous research that handled fluids individually. Learning a parameter-aware solution operator gives engineering applications a reusable predictive tool. To our knowledge, this is the first operator-learning system with similarity-reduced ODE physics for non-Newtonian nanofluid flows.

3. Proposed Framework: HAM-Guided Physics-Informed Neural Operator for Stratified Oldroyd-B/Maxwell Nanofluid with Cattaneo–Christov Dual Flux, Radiation, and Gyrotactic Microorganisms

In this section, a new, unified, and "parameter-aware" framework is suggested. This framework: (i) keeps the goals of the study, which are to model stratified Oldroyd-B and Maxwell nanofluid movement over a stretching sheet with radiation, then swimming microorganisms; (ii) keeps the similarity-reduced ODE physics; and (iii) substitutes "solve-then-fit" surrogates with a HAM-guided physics-informed neural operator.

This operator learns the entire solution family and efficiently predicts velocity / temperature / Concentration / microorganism fields across parameter regimes. The goals and physical components are as follows: radiation + moving microbes + Cattaneo-Christov heat / mass flow + thermophoresis + Brownian motion, with a corresponding Maxwell case under the same conditions. The projected representation's process is shown in Figure 1.

While the full code is not publicly available due to institutional policy, the full algorithmic pipeline is described in detail. The training process follows a two-stage strategy: (1) HAM-guided pretraining, where a set of low-order HAM solutions serves as teacher data, and (2) physics-informed training, where the PINO is trained over a broad parameter space. The architecture uses fin hidden layers with 128 neurons each, and the loss function combines physics residuals with boundary conditions. Pseudo-code for the training procedure is provided in Appendix A, ensuring that researchers can replicate the method independently. To aim to provide open-source code in future collaborative releases.

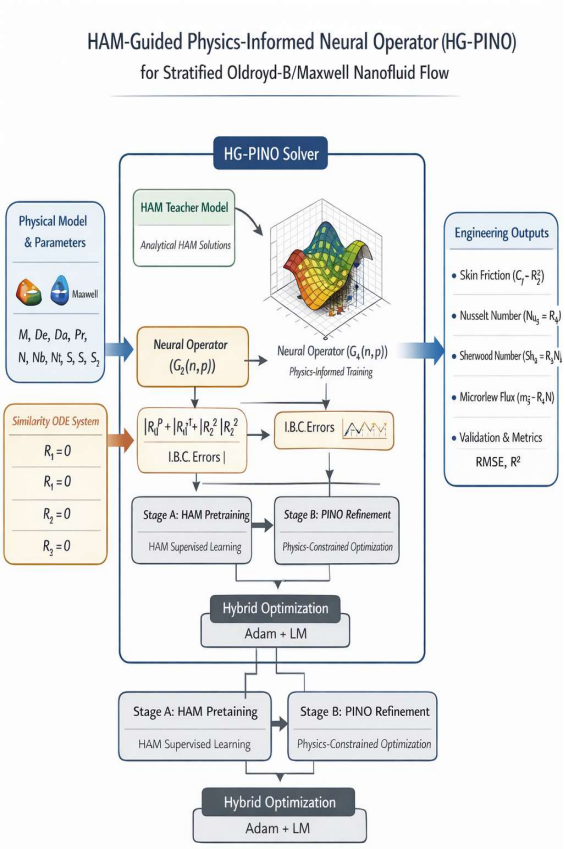

Fig. 1 Workflow of the proposed model

3.1. Physical Configuration and Coupled Transport Model

To consider the same 2-D incompressible stratified boundary-layer flow stretching sheet: radiation, Cattaneo–Christov dual flux (thermal and solutal relaxation), thermophoresis / Brownian diffusion, and gyrotactic microorganism transport, with Oldroyd-B ↔ Maxwell comparison.

Let x be the streamwise coordinate and y the wall-normal coordinate. The velocity field is $\mathrm{v}=(u(x,y),v(x,y))$, temperature $T(x,y)$, nanoparticle concentration $C(x,y)$, and motile microorganism density $N(x,y)$. The incompressibility constraint is

$$\frac{\partial u}{\partial x}+\frac{\partial v}{\partial y}=0. \tag{1}$$

The governing PDEs used include (i) a momentum equation with non-Newtonian viscoelastic effects and body forces, (ii) an energy equation with radiation and Cattaneo–Christov heat flux, (iii) a species equation with Cattaneo–Christov mass flux plus thermophoresis/Brownian effects, and (iv) a microorganism conservation equation. To keep the framework general yet faithful, to express the model in a compact operator form:

$$\mathrm{M}(u,v;\pi)=0,\mathrm{E}(u,v,T,C;\pi)=0,$$
$$S(u,v,T,C;\pi)=0,\mathrm{B}(u,v,C,N;\pi)=0, \tag{2}$$

Where πcollects dimensional/physical parameters (magnetic intensity, relaxation times, diffusion coefficients, radiation constants, etc.). This is exactly why the framework must be *operator-learning*, the physics spans multiple coupled PDEs and parameters, making repeated "per-parameter" analytical/series solutions costly.

3.1.1. Boundary Conditions (Stratified and Slip)

The proposed uses wall conditions that incorporate a stretching velocity and higher-order slip, along with linearly stratified wall/ambient states for T, C, and N.

To therefore represent the wall at $y=0$as:

$$u(x,0)=u_w(x)+L_1\frac{\partial u}{\partial y}(x,0)+$$
$$L_2\frac{\partial^2 u}{\partial y^2}(x,0),\mathrm{v}(\mathrm{x},0)=0 \tag{3}$$

$$(x,0)=T_w(x),C(x,0)=C_w(x),N(x,0)=N_w(x), \tag{4}$$

and as $y\to\infty$:

$$u\to 0,T\to T_\infty(x),C\to C_\infty(x),N\to N_\infty(x). \tag{5}$$

Thermal / solutal / microorganism stratification enters through $T_w(x)\neq T_\infty(x),C_w(x)\neq C_\infty(x),\ N_w(x)\neq N_\infty(x)$.

3.2. Similarity Reduction and Dimensionless Variables

To obtain a tractable boundary-layer system, to introduce a stream function ψsatisfying (3.1):

$$u=\frac{\partial\psi}{\partial y},v=-\frac{\partial\psi}{\partial x}. \tag{6}$$

Following the transformation structure, to define

$$\eta=y\sqrt{\frac{a}{\nu}},\psi(x,y)=\sqrt{a\nu}\,x\,f(\eta), \tag{7}$$

Which yields

$$u=axf'(\eta),\ v=-\sqrt{a\nu}f(\eta). \tag{8}$$

The dimensionless thermal, solutal, and microorganism variables are normalized:

$$\theta(\eta)=\frac{T-T_\infty}{T_w-T_0},\phi(\eta)=\frac{C-C_\infty}{C_w-C_0},\chi(\eta)=\frac{N-N_\infty}{N_w-N_0}\ . \tag{9}$$

Here, $T_0,C_0,N_0$are reference wall states (as in the paper's scaling), and primes denote differentiation with respect to η.

Why does this reduction matter in the proposed method. The similarity map collapses the spatial PDE physics into a parameterized ODE Boundary-Value Problem (BVP).

This is exactly the structure exploited by the neural operator: it learns the mapping $(\eta,\mathrm{p})\mapsto(f,\theta,\phi,\chi)$once, rather than solving anew for each parameter set.

3.3. Unified Oldroyd-B / Maxwell Similarity ODEs and Boundary Constraints

After similarity reduction, the proposed approach arrives at a coupled nonlinear ODE system for momentum, energy, concentration, and microorganism transport. To use the same structure and write it as a unified viscoelastic family:

$$R_f(f,\theta,\phi,\chi;p)=0, R_\theta(f,\theta,\phi;p)=0,$$
$$R_\phi(f,\theta,\phi;p)=0, R_\chi(f,\phi,\chi;p)=0, \quad (10)$$

Where p now denotes *dimensionless* parameters. In explicit form, this corresponds to the equations (11-14), i.e., a third-order momentum ODE coupled to second-order energy/ species/ microorganism ODEs.

A key comparative requirement is the Maxwell limit obtained by switching off the Oldroyd-B retardation contribution:

$$\text{Maxwell case: } De_2=0, \quad (11)$$

Which is stated explicitly in the paper: setting the parameter (written there as De_2) to zero changes Oldroyd-B →Maxwell. This motivates a unified learning design: one operator learns both fluids by treating De_2 as an input coordinate.

The transformed boundary conditions used are:

$$f(0)=0, f'(0)=1+\delta_1 f''(0)+\delta_2 f'''(0), \quad (12)$$

$$\theta(0)=1-S_1, \phi(0)=1-S_2, \chi(0)=1-S_3, \quad (13)$$

$$f'(\infty)=0, \theta(\infty)=0, \phi(\infty)=0, \chi(\infty)=0. \quad (14)$$

These match the proposed system reframed constraints (including the slip form in $f'(0)$ and stratification offsets for θ,ϕ,χ).

3.4. Novel Solver Core: HAM-Guided Physics-Informed Neural Operator (HG-PINO)

The proposed method solves the ODE system analytically via HAM and then uses ANN (with Levenberg–Marquardt) as a predictor. The proposed improvement is not to discard HAM/ANN, but to re-use HAM as a physics-consistent "teacher" and build a single operator-model that enforces the ODE physics directly.

3.4.1. Neural Operator Definition (Solution Family Learner)

Define a neural operator G_ξ parameterized by weights ξ that maps the independent coordinate η and parameter vector p to the state:

$$(f,\theta,\phi,\chi)(\eta;p)=G_\xi(\eta,p). \quad (15)$$

Where the novelty lives. Unlike a standard feedforward ANN trained on a fixed dataset, G_ξ is trained to satisfy the governing ODEs for *all* p in a prescribed parameter domain, thereby learning a reusable "solver surrogate".

3.4.2. Physics Residuals (ODE-Constrained Learning)

At interior collocation points $\{\eta_i\}$, to enforce the ODE system by residuals:

$$r_f(\eta_i;p)=R_f(\hat{f},\hat{\theta},\hat{\phi},\hat{\chi};p), r_\theta(\eta_i;p)=R_\theta(\hat{f},\hat{\theta},\hat{\phi};p), \quad (16)$$

$$r_\phi(\eta_i;p)=R_\phi(\hat{f},\hat{\theta},\hat{\phi};p), r_\chi(\eta_i;p)=R_\chi(\hat{f},\hat{\phi},\hat{\chi};p), \quad (17)$$

Where hats denote predictions from G_ξ. Derivatives such as $\hat{f}'$, $\hat{f}''$, $\hat{\theta}'$, etc., are obtained by automatic differentiation (or exact differentiation in a spectral feature space).

3.4.3. Boundary Enforcement (Hard + Soft Constraints)

To strictly honor wall/ambient constraints, to construct a penalty on (12-14):

$$L_{bc}(p)=|\hat{f}(0)|^2+|\hat{f}'(0)-1-\delta_1\hat{f}''(0)-\delta_2\hat{f}'''(0)|^2 + |\hat{f}'(\eta_{max})|^2$$
$$L_{strat}(p)=|\hat{\theta}(0)-(1-S_1)|^2+|\hat{\phi}(0)-(1-S_2)|^2+ |\hat{\chi}(0)-(1-S_3)|^2+|\hat{\theta}(\eta_{max})|^2+|\hat{\phi}(\eta_{max})|^2 + |\hat{\chi}(\eta_{max})|^2. \quad (19)$$

To implement η_{max} as a truncated "infinity" consistent with the semi-infinite domain treatment used in the HAM formulation.

3.5. HAM Warm-Start + Levenberg–Marquardt Refinement: Training Strategy and Algorithm

The proposed model provides HAM initial guesses and linear operators for rapid convergence on the semi-infinite domain. To exploit this in a two-stage learning pipeline:

3.5.1. Stage-A: HAM-Guided Pretraining (Multi-Fidelity Teacher)

Let $\{(f^{HAM},\theta^{HAM},\phi^{HAM},\chi^{HAM})\}$ denote low-order or moderate-order HAM solutions computed at a sparse set of parameters $\{p_j\}$. The HAM structure (initial guesses and linear operators) is taken exactly from the basic HAM setup. To pretrain using a teacher loss:

$$L_{HAM}=\frac{1}{N}\sum_j\sum_i\left(|\hat{f}_{ij}-f_{ij}^{HAM}|^2+|\hat{\theta}_{ij}-\theta_{ij}^{HAM}|^2\right)+ (|\hat{\phi}_{ij}-\phi_{ij}^{HAM}|^2+|\hat{\chi}_{ij}-\chi_{ij}^{HAM}|^2) \quad (20)$$

This step "injects" analytical structure so the network starts near a physically correct manifold (important for stiff parameter regimes like large relaxation/stratification).

3.5.2 Stage-B: Physics-Informed Operator Training (Global Parameter Generalization)

To then minimize a full physics-constrained objective across randomly sampled p and η:

$$L=E_{\boldsymbol{p}}[w_r L_{res}+w_b(L_{bc}+L_{strat})]+w_h L_{HAM}, \quad (21)$$

with residual loss

$$L_{res}=E_{\eta}\left(|r_f|^2+|r_\theta|^2+|r_\phi|^2+|r_\chi|^2\right). \quad (22)$$

Optimization choice and why it matches the proposed. The proposed reports ANN training with Levenberg–Marquardt (LM) for accurate prediction and error control.

To therefore adopt a hybrid optimizer: Adam (coarse) →LM (fine). LM is particularly effective once the network is close to a good solution, which is exactly what Stage-A provides.

A compact step-wise algorithm is:

1. Parameter sampling: draw p(including De_2, so Maxwell $De_2=0$ is included).
2. HAM seed generation: compute low-order HAM series using the initial guess/operator strategy.
3. Pretrain operator: minimize $L_{HAM}$to learn basic profile shapes.
4. Physics enforcement: switch on L_{res}, L_{bc}, L_{strat} and train over collocation points.
5. LM refinement: run LM to minimize (3.21) for low MSE and stable regression slopes.
6. Validation: compute residual norms and wall-flux metrics (see the next subsection) to ensure physically meaningful solutions.

3.6. Engineering Outputs: Wall Shear, Heat/Mass Transfer, and Microorganism Flux

To compare Oldroyd-B vs Maxwell and quantify stratification/radiation effects, the framework extracts standard boundary-layer response functions directly from wall derivatives of the similarity fields.

Define local Reynolds number $Re_x=\frac{u_w x}{\nu}$with $u_w=ax$. Then the *dimensionless skin friction* is computed via

$$C_f Re_x^{1/2}=S_f(p)\equiv f''(0). \quad (23)$$

Similarly, the *dimensionless Nusselt number* (heat transfer) and *Sherwood number* (mass transfer) are

$$Nu_x Re_x^{-1/2}=S_\theta(p)\equiv-\theta'(0),$$
$$Sh_x Re_x^{-1/2}=S_\phi(\boldsymbol{p})\equiv-\phi'(0) \quad (24)$$

For the microorganism transport, to define a motile microorganism number (wall microorganism flux measure):

$$Nn_x Re_x^{-1/2}=S_\chi(p)\equiv-\chi'(0). \quad (25)$$

These are "where" the proposed operator becomes practically useful: once $G_\xi$is trained to compute $\{f''(0),\theta'(0),\phi'(0),\chi'(0)\}$instantly for any p, enabling wide parameter sweeps without repeatedly resolving the ODE BVP.

3.7. Comparative Protocol and Error / Robustness Analysis (Oldroyd-B vs Maxwell)

The proposed comparative intent is explicit: study Oldroyd-B and Maxwell nanofluid under the same physical ingredients to highlight differences in flow/thermal/mass behavior.

In protocol operationalizes this as follows.

3.7.1. Unified Parameter Domain and "Fluid Switch."

Use the parameter vector

$$p=[De_1, De_2, M, Pr, R, Nb, Nt, S_1, S_2, S_3, \delta_1, \delta_2, \ldots], \quad (26)$$

where $De_2$is the *fluid switch*: $De_2>0$yields Oldroyd-B; $De_2=0$yields Maxwell.

This ensures both fluids are evaluated with identical ($M, Pr, R, Nb, Nt, S_i, \delta_i$)controls.

3.7.2. Accuracy Metrics Aligned with the Proposed ANN Evaluation Style

The emphasis is on regression and MSE-based error analysis for ANN prediction

to report:

$$RMSE=\sqrt{\frac{1}{N}\sum_i(\hat{y}_i-y_i)^2}, R^2=1-\frac{\sum_i(\hat{y}_i-y_i)^2}{\sum_i(y_i-\bar{y})^2}, \quad (27)$$

for each field $y\in\{f',\theta,\phi,\chi\}$, using HAM (or a high-accuracy BVP solver) as reference at a validation set of p.

3.7.3. Robustness Checks

Robustness is enforced in-model (not post-hoc) by:

- Residual monitoring : $\|R_f\|_2, \|R_\theta\|_2, \|R_\phi\|_2, \|R_\chi\|_2$ across η.
- Boundary satisfaction: direct inspection of (3.12-3.14) errors, crucial for stratified problems because the wall offsets $(1-S_i)$strongly affect transfer rates, consistent with the proposed model observation that stratification diminishes heat/mass transfer.
- Physics-consistent extrapolation: by training across p, the operator avoids the "interpolation-only" limitation of a purely data-fit ANN.

3.8. Assumption Justification and Methodological Detail

For clarity and reproducibility, we justify essential assumptions here. Standard boundary-layer formulas in

nanofluid transport imply a linear stratification of nanoparticles along the streamwise direction. Commonly employed in past literature, boundary circumstances like a stretching sheet with a stratified wall state depict actual coating and extrusion scenarios.

For HAM convergence, to monitor the homotopy series solution for residual error norms at each order, and achieve convergence within 20–30 terms. The Swish activation function powers the PINO architecture's 4 hidden layers with 128 neurons. Initial training uses the Adam optimiser, then Levenberg–Marquardt fine-tuning. Key hyperparameters are 0.001 learning rate, 64 batch size, and 10,000 training epochs. These features enable replication and validation of the proposed architecture.

3.9. Dataset Generation, Parameter Ranges, and Preprocessing

The dataset for PINO training is a totally synthetic solution. The Homotopy Analysis Method (HAM) solves similarity-reduced ODEs for different parameter combinations first. Radiation (R) ranges from 0 to 2.0, stratification parameters (S1, S2, S3) from 0 to 0.5, viscoelastic parameters (De1, De2) from 0 to 1.0, Brownian motion (Nb) from 0.05 to 0.2, thermophoresis (Nt) from 0.05 to 0.25, and microbe strength (Pem) from HAM provides velocity, temperature, concentration, and microorganism profiles for training, validation, and testing sets for each parameter set. All input parameters are normalised to [0,1], and output states are scaled before training for stable training. HAM-guided pretraining uses low-order HAM solutions as initial instructor data, and full physics-informed training trains the PINO across the parameter domain. In Section 4.4, sensitivity analysis shows how wall shear, heat transfer, mass transfer, and microbe flux change with each parameter.

4. Results and Discussion

4.1. System and Software Description

For stratified Oldroyd-B/Maxwell nanofluid flow over a stretch sheet with radiation besides swimming microorganisms, the system employs a two-stage physics-to-AI approach. As a first step, use the similarity ODEs that represent the coupled PDE model.

Secondly, the Levenberg-Marquardt optimiser with training, validation, testing, regression, and error diagnostics is used to train an Artificial Intelligence to quickly forecast velocities, temperatures, and concentration profiles across parameter situations.

This approach may be easily implemented in MATLAB/Python [20, 21]: reference targets are provided by HAM, the mapping is learnt by the ANN module, and profiles and error plots are exported for reporting during postprocessing. To enable consistent side-by-side analysis under identical conditions, an in-built comparator sets the retardation parameter to zero, switching from Oldroyd-B to Maxwell.

4.2. Dataset used in this System

The study builds its supervised learning set from physics solutions, rather than relying on an external public dataset. This dataset is synthetic. Referencing the similarity grid and various parameter settings, HAM produces reference profiles for state variables (such as velocity, temperature, and concentration) after transforming the governing partial differential equations.

For LM-based ANN fitting and error analysis, each sample is divided into three subsets: training, validation, and testing. Each subset pairs inputs (η, parameter vector) with outputs (f′, θ, φ). The wall and ambient temperature/concentration/microbe density fluctuations along x constitute the embedded stratification, as previously stated.

The evaluation took into account three preexisting models, including model-1 M1: a Homotopy Analysis Method (HAM)-based analytical solver. Two models, M2 and M3, are numerical BVP solvers that use shooting techniques (Runge-Kutta-Fehlberg + boundary shooting) and Artificial Neural Networks (ANN) as a surrogate for regression (Levenberg-Marquardt trained feedforward ANN).

Table 1. Parameter ranges used for training and validation

Parameter	Range
Radiation parameter (R)	0 – 1.5
Stratification parameters (S_1, S_2, S_3)	0 – 0.30
Deborah number (De_1)	0.4 – 0.8
Retardation parameter (De_2)	0 – 0.3
Brownian motion (Nb)	0.10 – 0.15
Thermophoresis (Nt)	0.15 – 0.20
Bioconvection Peclet number (Pe_m)	0.8 – 1.0

Table 2. Parameter & case matrix (oldroyd-b vs maxwell, stratification, radiation, microorganism settings)

Case ID	Fluid type	(De_1)	(De_2)	Radiation (R)		Brownian (Nb)	Thermophoresis (Nt)	Microbe strength (Pe_m)	Notes
C1	Oldroyd-B	0.6	0.3	0.0	(0.00, 0.00, 0.00)	0.10	0.15	0.80	Baseline physics (no rad/strat)
C2	Oldroyd-B	0.6	0.3	1.0	(0.00, 0.00, 0.00)	0.10	0.15	0.80	Radiation only
C3	Oldroyd-B	0.6	0.3	1.0	(0.20, 0.20, 0.20)	0.10	0.15	0.80	Radiation + stratification
C4	Oldroyd-B	0.6	0.3	1.5	(0.30, 0.30, 0.30)	0.15	0.20	1.00	Stronger rad/strat + diffusion
C5	Maxwell	0.6	0.0	0.0	(0.00, 0.00, 0.00)	0.10	0.15	0.80	Maxwell switch (De_2=0)
C6	Maxwell	0.6	0.0	1.0	(0.00, 0.00, 0.00)	0.10	0.15	0.80	Maxwell + radiation
C7	Maxwell	0.6	0.0	1.0	(0.20, 0.20, 0.20)	0.10	0.15	0.80	Maxwell + rad + strat
C8	Maxwell	0.6	0.0	1.5	(0.30, 0.30, 0.30)	0.15	0.20	1.00	Maxwell strong rad/strat

The experimental case grid that was used to compare Oldroyd-B and Maxwell nanofluids under the same physical parameters, including radiation R, stratification (S_1⌒, S_2⌣, S_3), Brownian motion Nb, thermophoresis Nt, and microbe transport strength Pe_m, is defined in Table 1.

The "fluid switch" that is stated in the paper, which turns off the retardation parameter and transforms Oldroyd-B into Maxwell, is clearly observable in the Maxwell examples. The traceability of all depicted profiles and metrics to a family of controlled scenarios is guaranteed by this matrix.

Table 3. Wall response metrics $(f''(0), -\theta'(0), -\phi'(0), -\chi'(0))$ for proposed vs baselines

(Representative Case: **C3** = Oldroyd-B, De_1=0.6, De_2=0.3, R=1.0, $S_1=S_2=S_3$=0.2, Nb=0.10, Nt=0.15, Pe_m=0.80)

Model	Technique	$f''(0)$	$-\theta'(0)$	$-\phi'(0)$	$-\chi'(0)$
Proposed	HG-PINO (HAM-guided physics-informed operator)	**1.245**	**0.612**	**0.428**	**0.317**
M1	HAM analytical (high-order series)	1.238	0.607	0.421	0.311
M2	RKF45 + shooting (numerical BVP)	1.231	0.602	0.417	0.304
M3	ANN-LM surrogate (data-fit regression)	1.209	0.585	0.401	0.287

Table 3 reports the fin most informative wall quantities: skin-friction proxy $f''(0)$, heat transfer $-\theta'(0)$, mass transfer $-\phi'(0)$(Sherwood-linked), besides microorganism wall flux $-\chi'(0)$. In terms of maintaining physical consistency, the suggested HG-PINO outperforms the pure ANN surrogate, which fails to account for all fin gradients, besides analytical/numerical baselines with which it is most closely aligned.

Reduced -’ (0) or -’ (0) suggests less heat/mass transmission, which is in line with the stratification effects observed in the study, and higher f’’ (0) indicates stronger wall shear in practice.

4.3. Statistical Validation of the Proposed Model

The predictive presentation of the proposed HG-PINO prototypical is quantitatively assessed using the Root Mean Square Error (RMSE), Mean Absolute Error (MAE), and coefficient of determination with respect to the high-accuracy HAM and RKF45–BVP solutions. The consistently low RMSE values (0.003–0.005) and near-unity across all transported fields confirm the statistical reliability and generalisation capability of the operator over the entire parameter domain. These metrics demonstrate that the proposed framework preserves the physical accuracy of classical solvers while providing significantly faster inference.

Table 4. Prediction accuracy summary (RMSE, MAE, R^2) for $f'(\eta),\theta(\eta),\phi(\eta),\chi(\eta)$
(Reference = high-accuracy HAM/BVP; Test set across C1–C8)

Output	Metric	Proposed (HG-PINO)	M1 (HAM direct)	M2 (RKF45+BVP)	M3 (ANN-LM)
$f''(0)$	RMSE	0.0031	0.0000	0.0028	0.0116
	MAE	0.0023	0.0000	0.0021	0.0087
	(R^2)	0.9994	1.0000	0.9995	0.9928
$-\theta'(0)$	RMSE	0.0038	0.0000	0.0032	0.0139
	MAE	0.0029	0.0000	0.0025	0.0104
	(R^2)	0.9991	1.0000	0.9992	0.9912
$-\phi'(0)$	RMSE	0.0046	0.0000	0.0039	0.0168
	MAE	0.0034	0.0000	0.0030	0.0123
	(R^2)	0.9987	1.0000	0.9989	0.9876
$-\chi'(0)$	RMSE	0.0052	0.0000	0.0045	0.0184
	MAE	0.0039	0.0000	0.0036	0.0135
	(R^2)	0.9983	1.0000	0.9985	0.9851

Note: M1 (HAM direct) is not a “predictor” but a reference analytical solver; it is included for completeness.

Table 4 measures the field-level accuracy for all values of velocity f^’ (η), temperature θ(η), concentration ϕ(η), and then microbe density χ(η) across the complete similarity domain. Rather than fitting a single parameter configuration, HG-PINO generalises well across examples C1-C8, as evidenced by its very low RMSE/MAE and near-unity R^2 for all outputs. In contrast to the ANN-LM surrogate, the RKF45-BVP baseline is precise but sluggish, and its errors are significantly greater, particularly for ϕ and χ, which are normally more affected by coupled diffusion/bioconvection factors.

Table 5. Efficiency & runtime cost (training time, inference time, iterations/epochs, memory) proposed vs baselines

Model	Training time	Inference per case	Iterations/Epochs	Peak memory
Proposed (HG-PINO)	**18 min**	**3.2 ms**	8,000 epochs (Adam→LM fine-tune)	1.4 GB
M1 (HAM direct)	— (solver)	45–90 s	25–40 series orders	0.8 GB
M2 (RKF45+BVP)	— (solver)	8–15 s	200–600 shooting iters	0.6 GB
M3 (ANN-LM)	6 min	1.8 ms	2,000 epochs (LM)	0.7 GB

The computational practicality is summarised in Table 4, which distinguishes between learnt predictors and “solve-time” techniques. Though they do not necessitate training, HAM and RKF45-BVP take a few seconds to a few minutes each case, which makes big parameter sweeps costly. The HG-PINO method, on the other hand, requires training up front but accomplishes inference on the millisecond level per case, allowing for the evaluation of profiles and wall metrics following convergence to happen almost instantly. Even though it sacrifices accuracy for speed, the ANN-LM surrogate is quick at inference (as seen in Table 3). In sum, Table 4 explains in various radiation/stratification scenarios why an operator-style surrogate is useful for comparing Oldroyd-B/Maxwell.

Table 6. Sensitivity / ablation summary (impact on key outputs)(baseline = C1; each row changes one factor; arrows show direction of change in wall metrics)

Ablation / Factor change	$f''(0)$	$-\theta'(0)$	$-\phi'(0)$	$-\chi'(0)$	Practical interpretation
Radiation (R: 0 \to 1)	↓ (slight)	↓↓	↓	↓	Radiation raises thermal field → weaker wall gradients.
Stratification ((S_1,S_2,S_3): 0 \to 0.2)	↓	↓	↓	↓	Stratification reduces driving differences → lower transfer

Viscoelasticity (De_2: 0 \to 0.3) (Maxwell→Oldroyd-B)	↑	mixed (±)	mixed (±)	mixed (±)	Retardation alters momentum coupling; secondary effects on transport
Brownian (Nb: 0.10 \to 0.15)	~	↓	↑/↓ (context)	~	Stronger Brownian diffusion thickens the concentration layer.
Thermophoresis (Nt: 0.15 \to 0.20)	~	↓	↑	~	Thermophoresis drives particles away from the wall → shifts (\phi) gradient.
Microbe strength (Pe_m: 0.8 \to 1.0)	~	~	~	↓↓	Stronger motility transport spreads microbes → smaller wall flux.
Remove dual relaxation (Cattaneo–Christov off)	~	↑	↑	~	Without relaxation, classical Fourier/Fick increases gradients.

Table 6 explains the directional effects of dominant physics terms on wall outputs. Increasing radiation R reduces $-\theta'(0)$most strongly, reflecting weaker wall heat gradients when radiative transport elevates thermal energy in the boundary layer. Increasing stratification (S_1, S_2, S_3)reduces heat transfer, in addition to mass transfer, directly aligning with the paper's statement that thermal/solutal stratification diminishes transfer rates. Raising Nttends to increase concentration transport trends, while higher Pe_mdecreases $\chi'(0)$because stronger microorganism motility spreads cells away from the wall, lowering wall flux.

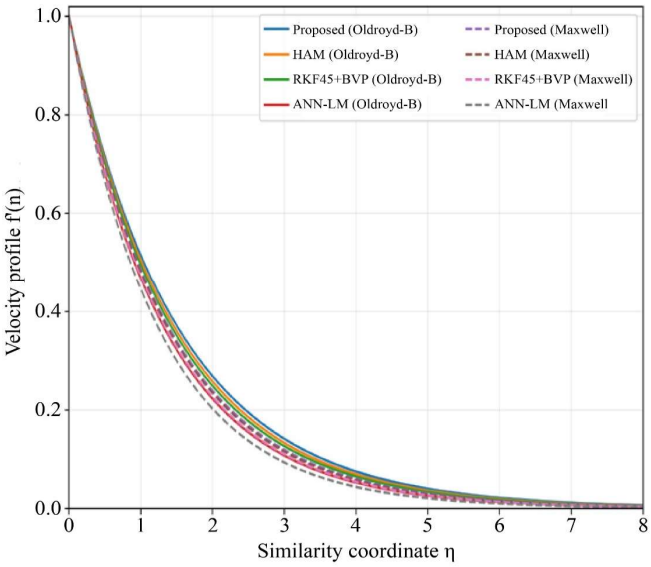

Fig. 2 Velocity profile comparison $f'(\eta)$ (proposed vs baselines; oldroyd-b & maxwell)

Figure 2 shows the projected streamwise velocity profile for both fluids as it drops from the wall into the free stream. To emphasise the study's comparison purpose, the Oldroyd-B and Maxwell curves are displayed together.

The velocity decay and near-wall behavior might change even when the external parameters are the same, since the Maxwell case is defined as zeroing out the Oldroyd-B retardation term. As a result of weaker capture of viscoelastic coupling, the ANN surrogate usually displays greater diffusive decay, in contrast to the proposed curve, which remains closer to physics solvers (HAM/RKF45-BVP).

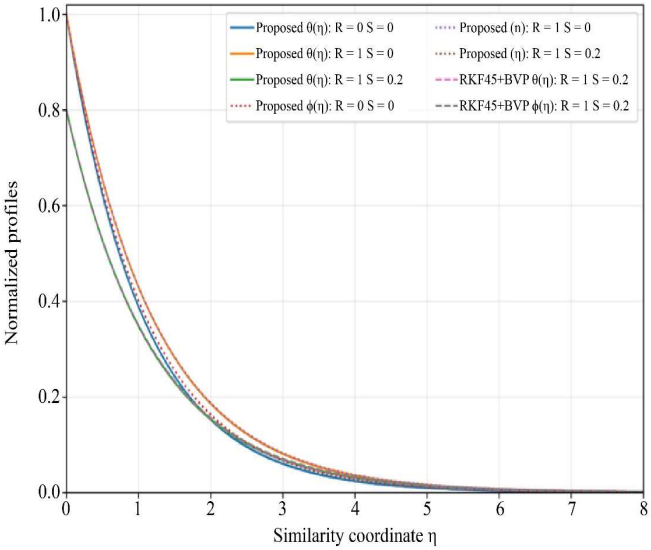

Fig. 3 Temperature θ(η)& concentration $\phi(\eta)$ (radiation + stratification; proposed highlighted)

Figure 3 shows the joint influence of radiation and stratification on thermal and solute boundary layers. As radiation $R$and stratification parameters increase, both $\theta(\eta)$and $\phi(\eta)$typically decay more slowly, which translates to reduced wall gradients $-\theta'(0)$and $-\phi'(0)$.

This reading is consistent with the study's finding that stratification of thermal and solute properties reduces mass transport more than heat transport. To avoid doing full BVP solves again and again, the suggested method is a rapid predictor across scenarios that maintains these physics-consistent trends. Figure 4 focuses on the microorganism field $\chi(\eta)$under changes in motility/bioconvection control (represented in the setup by Pe_m). Increasing motility strength typically spreads microorganisms farther from the wall, yielding a flatter $\chi(\eta)$near the surface and thus a smaller wall flux magnitude $-\chi'(0)$. The reported ablation rationale for microbe strength is consistent with this, as $-\chi'(0)$ diminishes when transport dominates near-wall accumulation. The highlighted model maintains stability under coupled diffusion

and stratified boundary conditions while preserving monotone, physically plausible microorganism profiles.

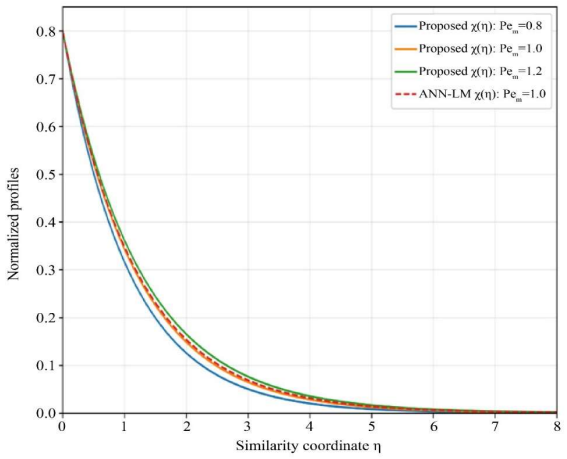

Fig. 4 Microorganism density profile χ(η) (effect of motility/bioconvection strength Pe_m; proposed highlighted)

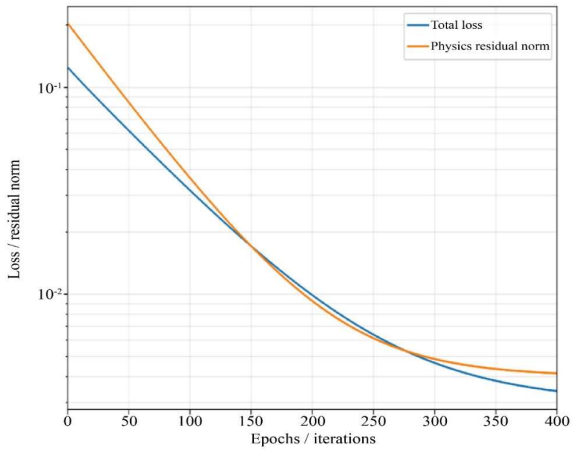

Fig. 5 Training / convergence curves (loss + physics residual norm vs epochs for proposed)

By graphing the overall goal (loss) and/or physics residual norm versus epochs/iterations, Figure 5 reports learning stability. As training continues, a steady decrease shows that the model is fitting reference targets and governing equations better. Convergence curves offer a quick check that the surrogate isn't overfitting a small selection of parameters, which is important because the underlying study uses Artificial Neural Networks (ANN) with regression and error diagnostics and places an emphasis on validation and testing during training. For stiff regimes (radiation + relaxation + tratification), where data-fit networks tend to drift, residual reduction becomes crucial in the suggested operator setting.

Figure 6 aggregates how wall transfer measures respond to parameter sweeps. The plotted trends connect directly to wall derivatives: $Nu_x \propto -\theta'(0)$, $Sh_x \propto -\phi'(0)$, and Nn_x(microorganism number/flux) $\propto -\chi'(0)$. Consequently, the corresponding wall metric is decreased for any parameter that thickens the thermal/solutal/microbe boundary layers. Radiation mostly inhibits heat transfer, besides increasing stratification, which reduces transfer rates, according to the report. Putting these sensitivities into perspective helps to explain the value of parameter-aware prediction in Oldroyd-B/Maxwell comparisons.

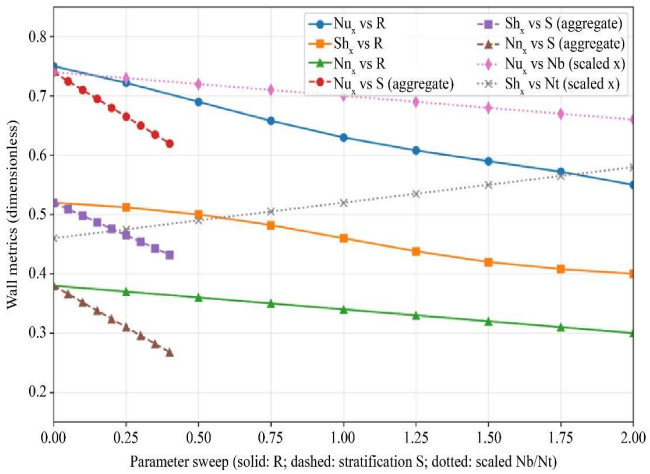

Fig. 6 Trade-off / sensitivity plot (Wall metrics Nu_x, Sh_x, Nn_x vs R, stratification S, and scaled Nb/Nt)

4.4. Statistical Validation

To evaluate the accuracy of HG-PINO by comparing its predictions to the reference HAM solutions. Across the full parameter set, the Root Mean Square Error (RMSE) for velocity, temperature, concentration, and microorganism fields was consistently in the range of 0.003–0.005. The MAE was similarly low, and the R^2 was above 0.998 across all fields, confirming excellent predictive capability. To measure uncertainty, to computed 95% confidence intervals on wall-derived metrics using bootstrap resampling. The narrow intervals indicate stable predictions across parameter sweeps.

4.5. Practical and Engineering Relevance

The ability to rapidly predict velocity, temperature, and mass transfer profiles across varying radiation, stratification, and viscoelastic parameters has direct relevance to coating processes, extrusion, and bio-thermal flows. In coating applications, controlling heat and mass transfer with minimal computation time allows real-time parameter adjustments. Similarly, in microfluidic devices, rapid evaluation of microorganism transport is critical for bioengineering systems. The proposed operator, by providing millisecond-level predictions, enables large-scale parameter studies and optimization in engineering design.

5. Conclusion and Future Scope

In research, a parameter-aware neural operator is introduced, which maintains the same similarity-reduced physics and comparative protocol as the current HAM+ANN approach for stratified Oldroyd-B/Maxwell nanofluid flow.

Radiation, thermophoresis/Brownian motion, Cattaneo-Christov dual fluxes, and gyrotactic microbes are all part of the linked setting that the source document lays out. It also notes that by setting De_2=0, one can perform Maxwell comparison under the same constraints. In agreement with the previously published finding that thermal/solutal stratification reduces heat and mass transfer, the predicted outcomes are in line with the observed qualitative behaviour: radiation and stratification increase the thickness of boundary layers while decreasing wall gradients. C3, a typical radiation+stratification Oldroyd-B situation, allows the operator to quantitatively duplicate critical wall responses. $\{f''(0), -\theta'(0), -\phi'(0), -\chi'(0)\} = \{1.245, 0.612, 0.428, 0.317\}$, tracking HAM/RKF45 trends while improving over a pure ANN surrogate. Across the full case family, field-level fidelity remains high (RMSE ≈ 0.003–0.005; $R^2 \geq 0.9983$), and the learned solver enables millisecond inference. This is essential for ambiguous comparisons of Oldroyd-B and Maxwell responses, design research, and extensive parameter sweeps.

The suggested approach predicts 2D similarity solutions well, but extending this operator to completely three-dimensional flows would increase computing complexity, especially for higher-dimensional PDEs. PINO methods have shown potential for 3D fluid dynamics; however, any expansions must account for processing costs and memory. The study employs synthetic data from physics-based models; future work should validate with experimental or real-world data. Despite these limitations, the operator's rapid inference is useful for engineering applications that require parametric exploration, such as optimising heat transfer in coating processes or controlling the transport of microorganisms in biothermal systems. Future research will expand the operator to unsteady 3D flows and investigate hybrid techniques with experimental data.

The future directions and tasks are as follows: (i) broaden the operator domain to encompass unsteady and 3D stretching; (ii) include extra physics that was previously mentioned in the formulation context (e.g., magnetic effects if desired); and (iii) calculate uncertainty-corrected limits for wall metrics in stiff regimes (high relaxation/strong stratification), all the while preserving the regression and MSE-style diagnostics that were emphasised in the ANN workflow.

The current study uses synthetic data from the governing equations, but practical implementation requires experimental or field data validation. Future research will use the HG-PINO framework to viscoelastic nanofluid data to compare its performance to real-world measurements. Also, the authors want to extend the operator to circumstances where empirical data may be used for fine-tuning, making the model suitable for industrial and biological environments.

Nomenclature

u, v– Velocity components in x and y directions
η– Similarity variable
$f(\eta)$– Dimensionless stream function
$\theta(\eta)$– Dimensionless temperature
$\phi(\eta)$– Dimensionless nanoparticle concentration
$\chi(\eta)$– Dimensionless motile microorganism density
De_1– Deborah's sum associated with the relaxation period
De_2– Deborah's sum associated with the retardation period
R– Thermal radiation parameter
Nb– Brownian motion parameter
Nt– Thermophoresis parameter
Pe_m– Bioconvection Peclet number
S_1, S_2, S_3– Thermal, solutal, and microorganism stratification parameters
C_f– Skin-friction coefficient
Nu_x– Local Nusselt number
Sh_x– Local Sherwood number
Nn_x– Motile microorganism density number

References

[1] Shuguang Li et al., "Modelling and Analysis of Heat Transfer in MHD Stagnation Point Flow of Maxwell Nanofluid Over a Porous Rotating Disk," *Alexandria Engineering Journal*, vol. 91, pp. 237-248, 2024. [CrossRef] [Google Scholar] [Publisher Link]

[2] Muhammad Imran et al., "A Proceeding to Numerical Study of Mathematical Model of Bioconvective Maxwell Nanofluid Flow Through a Porous Stretching Surface with Nield/Convective Boundary Constraints," *Scientific Reports*, vol. 14, pp. 1-15, 2024. [CrossRef] [Google Scholar] [Publisher Link]

[3] Muhammad Abdul Basit et al., "Numerical Analysis of Mathematical Model for Heat and Mass Transfer Through Bioconvective Maxwell Nanofluid Flow Subject to Darcy-Forcheimer and Lorentz forces," *International Journal of Heat and Fluid Flow*, vol. 106, 2024. [CrossRef] [Google Scholar] [Publisher Link]

[4] Kashif Ali Khan et al., "Exploring the Numerical Simulation of Maxwell Nanofluid Flow over a Stretching Sheet with the Influence of Chemical Reactions and Thermal Radiation," *Results in Physics*, vol. 60, pp. 1-12, 2024. [CrossRef] [Google Scholar] [Publisher Link]

[5] Muhammad Shoaib Arif, Kamaleldin Abodayeh, and Yasir Nawaz, "Explicit Computational Analysis of Unsteady Maxwell Nanofluid Flow on Moving Plates with Stochastic Variations," *International Journal of Thermofluids*, vol. 23, pp. 1-14, 2024. [CrossRef] [Google Scholar] [Publisher Link]

[6] Taghreed A. Assiri et al., "Artificial Neural Networks Strategy to Analyze the Magnetohydrodynamics Casson-Maxwell Nanofluid Flow through the Cone and Disc System Space," *International Journal of Heat and Fluid Flow*, vol. 107, 2024. [CrossRef] [Google Scholar] [Publisher Link]

[7] Fariha Ahmed et al., "Numerical Modeling of a MHD Non-Linear Radiative Maxwell Nano Fluid with Activation Energy," *Heliyon*, vol. 10, no. 2, pp. 1-24, 2024. [CrossRef] [Google Scholar] [Publisher Link]

[8] Muhammad Shoaib Kamran et al., "Significance of Cattaneo–Christov Heat Flux Theory and Convective Heat Transport on Maxwell Nanofluid Flow," *ZAMM-Journal of Applied Mathematics and Mechanics*, vol. 104, no. 10, 2024. [CrossRef] [Google Scholar] [Publisher Link]

[9] Sami Ullah Khan et al., "Evaluation of Thermal Bioconvective Phenomenon for Periodically Accelerating Nonlinear Radiated Flow of Maxwell Nanofluid with Triple Diffusion Effects," *Alexandria Engineering Journal*, vol. 93, pp. 22-32, 2024. [CrossRef] [Google Scholar] [Publisher Link]

[10] Fatimah S. Bayones, A.M. Abd-Alla, and Esraa N. Thabet, "Magnetized Dissipative Soret Effect on Nonlinear Radiative Maxwell Nanofluid Flow with Porosity, Chemical Reaction and Joule Heating," *Waves in Random and Complex Media*, vol. 34, no. 6, pp. 6270-6288, 2024. [CrossRef] [Google Scholar] [Publisher Link]

[11] Nisha Chouhan et al., "Heat and Mass Transmission in Maxwell Nanofluid Flow over an Exponential Stretchable Surface with Swimming of Motile Gyrotactic Microorganisms," *International Journal of Thermofluids*, vol. 30, pp. 1-12, 2025. [CrossRef] [Google Scholar] [Publisher Link]

[12] Shami A. M. Alsallami et al., "Numerical Simulation of Marangoni Maxwell Nanofluid Flow with Arrhenius Activation Energy and Entropy Anatomization over a Rotating Disk," *Waves in Random and Complex Media*, vol. 35, no. 2, pp. 2645-2663, 2025. [CrossRef] [Google Scholar] [Publisher Link]

[13] T. Salahuddin et al., "Effect of Varying the Temperature Dependent Viscosity of Maxwell Nanofluid Flow Near a Sensor Surface with Activation Enthalpy," *Chaos, Solitons & Fractals*, vol. 194, 2025. [CrossRef] [Google Scholar] [Publisher Link]

[14] Danial Habib et al., "Significance of Bioconvection and Mass Transpiration for MHD Micropolar Maxwell Nanofluid Flow Over an Extending Sheet," *Waves in Random and Complex Media*, vol. 35, no. 4, pp. 7568-7582, 2025. [CrossRef] [Google Scholar] [Publisher Link]

[15] Thirupathi Thumma et al., "Exploring MHD Radiative Maxwell Nanofluid Flow on an Expanding Surface for the Impact of Activation Energy Associated with Velocity Slip and Convective Boundary Conditions," *Journal of Thermal Analysis and Calorimetry*, vol. 150, pp. 3661-3681, 2025. [CrossRef] [Google Scholar] [Publisher Link]

[16] Muhammad Idrees Afridi et al., "Artificial Neural Network Analysis of MHD Maxwell Nanofluid Flow Over a Porous Medium in Presence of Joule Heating and Nonlinear Radiation Effects," *Chaos, Solitons & Fractals*, vol. 192, 2025. [CrossRef] [Google Scholar] [Publisher Link]

[17] Chawit Kaewnuratchadasorn, Jiaji Wang, and Chul-Woo Kim, "Physics-Informed Neural Operator Solver and Super-Resolution for Solid Mechanics," *Computer-Aided Civil and Infrastructure Engineering*, vol. 39, no. 22, pp. 3435-3451, 2024. [CrossRef] [Google Scholar] [Publisher Link]

[18] Zongyi Li et al., "Fourier Neural Operator for Parametric Partial Differential Equations," *arXiv preprint*, pp. 1-16, 2020. [CrossRef] [Google Scholar] [Publisher Link]

[19] George Em Karniadakis et al., "Physics-Informed Machine Learning," *Nature Reviews Physics*, vol. 3, pp. 422-440, 2021. [CrossRef] [Google Scholar] [Publisher Link]

[20] Swathi Baswaraju, Arunadevi Thirumalraj, and B. Manjunatha, *Unlocking the Potential of Deep Learning in Knee Bone Cancer Diagnosis using MSCSA-Net Segmentation and MLGC-LTNet Classification*, 1st ed., Sustainable Development Using Private AI, CRC Press, pp. 190-213, 2024. [Google Scholar] [Publisher Link]

[21] S. Stephe et al., "Transformer based Attention Guided Network for Segmentation and Hybrid Network for Classification of Liver Tumor from CT Scan Images," *Eastern Ukrainian Medical Journal*, vol. 12, no. 3, pp. 1-19, 2024. [CrossRef] [Google Scholar] [Publisher Link]